Optics and Lasers in Engineering **18** (1993) 25–51

On the Sensitivity of Coherent Gradient Sensing: Part II—An Experimental Investigation of Accuracy in Fracture Mechanics Applications

Hugh A. Bruck & Ares J. Rosakis

Graduate Aeronautical Laboratories, California Institute of Technology, Pasadena, California 91125, USA

(Received 25 July 1991; revised version received 5 April 1992; accepted 18 April 1992)

ABSTRACT

The sensitivity of the transmission 'Coherent Gradient Sensing' (CGS) technique is investigated experimentally in relation to the study of deformations near the tips of cracks in three-point bend specimens. Fringe data from these experiments are interpreted as gradients (geometric interpretation) and finite differences (physical interpretation) of hydrostatic stress fields. These data are used to compare the accuracy of the geometric interpretation of fringes with the physical interpretation of fringes obtained using increased sensitivity in order to confirm the theoretical findings from Part I of this investigation. Also, a least-squares fitting technique was used on the fringe data obtained from the region outside of the near tip 3D zone in order to investigate issues of K-dominance of the stress field in this region.

Results from the experimental investigations reported in this paper indicated that increasing the sensitivity of the CGS technique improved the quantity and quality of fringe data. However, the apparent size of the region on the image plane dominated by 3D effects increased and the differences between the geometric and physical interpretations of CGS fringe data were increased as well. In addition, the stress field outside of the 3D zone was determined not to be strictly K-dominant, as was predicted by results from previous experiments.

1 INTRODUCTION

This paper outlines some recent advances in the interpretation and application of lateral shearing interferometers to the full field investi-

gation of crack tip deformations in transparent solids. The lateral shearing interferometer used in the experimental investigations outlined in this paper has been named the 'Coherent Gradient Sensor' (CGS).[1] This technique has been used to obtain in-plane stress gradient fields (transmission) and out-of-plane displacement gradient fields (reflection) at the tips of stationary cracks in PMMA and Al 6061 specimens[2] and at the tips of propagating cracks in PMMA and AISI 4340 carbon steel.[3] The data obtained from these experiments have been used to investigate the transient nature of fracture phenomena and the structure of three-dimensional (3D) effects near the crack tip. The purpose of these investigations has been to identify the conditions under which K-dominance prevails around crack tips.

The CGS technique has the same advantages as other lateral shearing interferometric techniques used to measure deformation fields, such as the speckle-shearing interferometers of Hung and Taylor[4] and Hung and Liang,[5] which are variations on the Wollaston Prism Interferometer. These advantages include: (1) insensitivity to ambient vibrations, (2) simple optical components to set up and align, (3) variable sensitivity, (4) direct full-field measurements of deformation gradients, and (5) excellent fringe quality. However, unlike the speckle-shearing interferometers which vary fringe sensitivity by using various small angle prisms or by adjusting the distance of the object relative to the imaging lens, the CGS technique alters sensitivity merely by adjusting the separation between a pair of diffraction gratings, which are used as the lateral shearing components of the interferometer. Thus, unlike the optical path problems that arise when using thick prisms or large object distances in speckle-shearing interferometers, the CGS technique *does not compromise* any of the optical quality or construction of the fringe patterns when certain ranges of sensitivity are desired. Furthermore, the CGS technique can provide measurements of orthogonal deformation gradients simultaneously with the use of cross-gratings.

In Part I of this investigation,[6] theoretical calculations of the errors in interpreting fringes as gradients were made for wave fronts perturbed by deformations due to K-dominant stress fields. Part II compares the finite difference (physical) interpretation and the gradient (geometric) interpretation of transmission CGS fringe fields using experimental data obtained near the tips of cracks in PMMA specimens. Also, a least-squares fit to the fringe data will be made using Williams' solution in order to determine K-dominance in the region outside of the near tip 3D zone.

2 EXPERIMENTAL DESCRIPTION

Three-point bend experiments were conducted using the transmission CGS technique described in Part I of this investigation and seen in Fig. 1. Single edge notched PMMA ($c = 1{\cdot}08 \times 10^{-4}\,\text{mm}^2/\text{N}$) specimens were prepared with the dimensions seen in Fig. 2. A crack length (a) to plate width (w) ratio of 0·2 was used to obtain a crack tip stress field that would most likely have some K-dominant region as indicated by results from experiments performed on similar plate geometries in Ref. 2. A larger plate width was used in these experiments than those performed in Ref. 2 in order to reduce possible boundary effects on the crack tip stress field. A band saw, approximately 1 mm thick, was used to cut notches in these specimens. A collimated He–Ne laser beam of diameter 50 mm was centered around the crack tip and transmitted through the specimens in these experiments. The perturbed wave front was then processed through a pair of line gratings of density 40 lines per mm.

Two sets of experiments were then conducted on the specimen. The first experiment was conducted at a grating separation distance $\Delta \cong 33$ mm. The resulting fringe sensitivity for the experimental parameters chosen is approximately 0·022°/fringe. The maximum deflection that could be measured was limited by the choice of aperture size to approximately 0·72°, and deflections greater than this do not reach the

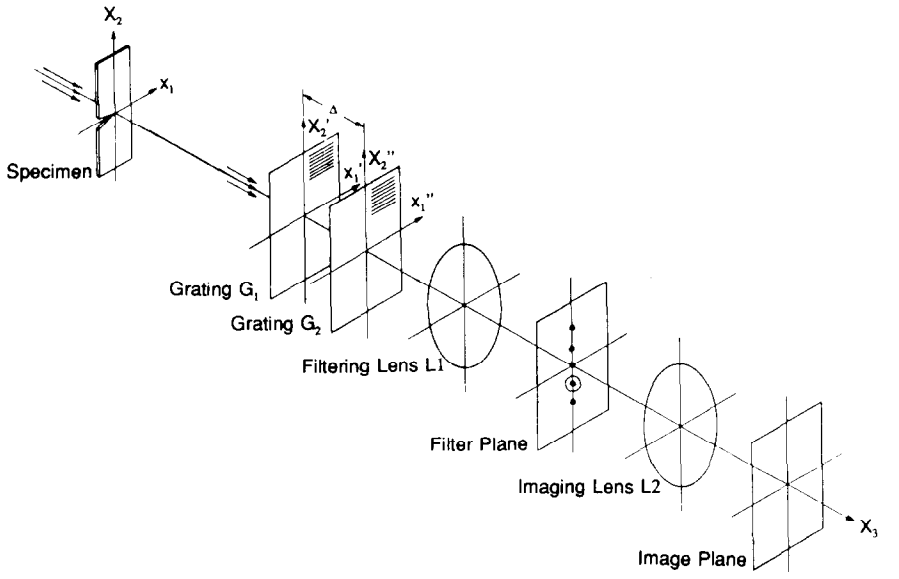

Fig. 1. Schematic of the experimental set-up for transmission CGS.

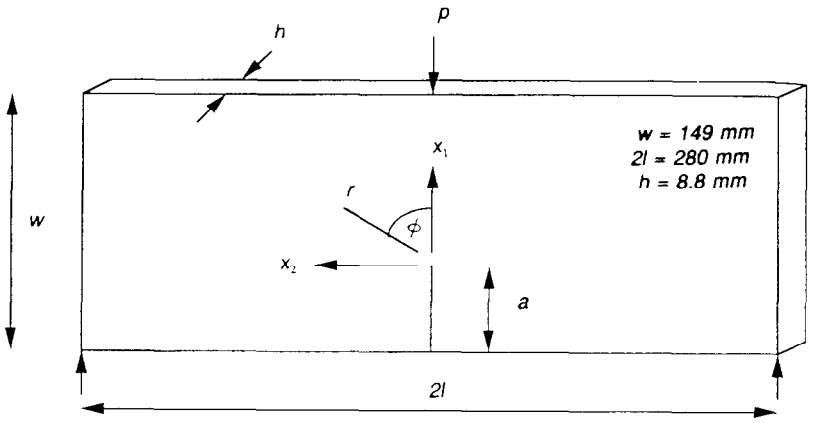

Fig. 2. Three-point bend fracture specimen.

image plane, leading to the formation of a small dark spot around the crack tip. A load of $P \cong 2230\,\text{N}$ was applied to the specimen, resulting in a calculated $K_I^{2D} \cong 1{\cdot}45\,\text{MPa}\sqrt{\text{m}}$.[7] Figure 3 shows the infinite width light fringe field around the crack tip when the grating lines are perpendicular to the x_1- and x_2-axes respectively, for an unloaded specimen. Figure 4 shows the fringes generated around the same crack tip when the specimen is loaded. From the characteristic dimensions of the plate $\left(\frac{w}{h} \cong 17\right)$, it is reasonable to assume that a state of plane stress may exist in a region surrounding the 3D zone near the crack tip, thereby predicating the use of the optical coefficient, c, in interpreting fringes in these regions as gradients of the applied stress field.

The second experiment was conducted on a plate with the same geometry and loading as in the first experiment. The grating separation used in this experiment was $\Delta \cong 100\,\text{mm}$. The corresponding fringe sensitivity for this grating separation was approximately 0·007°/fringe. Figure 5 shows the infinite width light fringe field around the crack tip when the grating lines are perpendicular to the x_1- and x_2-axes respectively, for an unloaded specimen. Figure 6 shows the fringes generated around the same crack tip when the specimen is loaded.

3 EXPERIMENTAL FRINGE DATA ANALYSIS

3.1 *K*-dominance in fringe interpretation

Using the K-dominant, geometric interpretation of transmission CGS fringes from Part I of this investigation, two functions $Y^{(1)}$ and $Y^{(2)}$ will

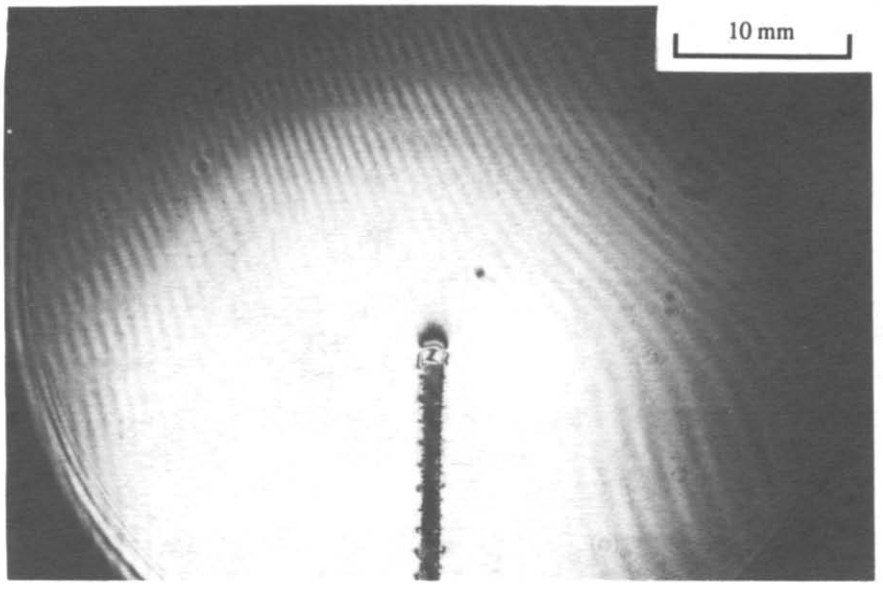

(a)

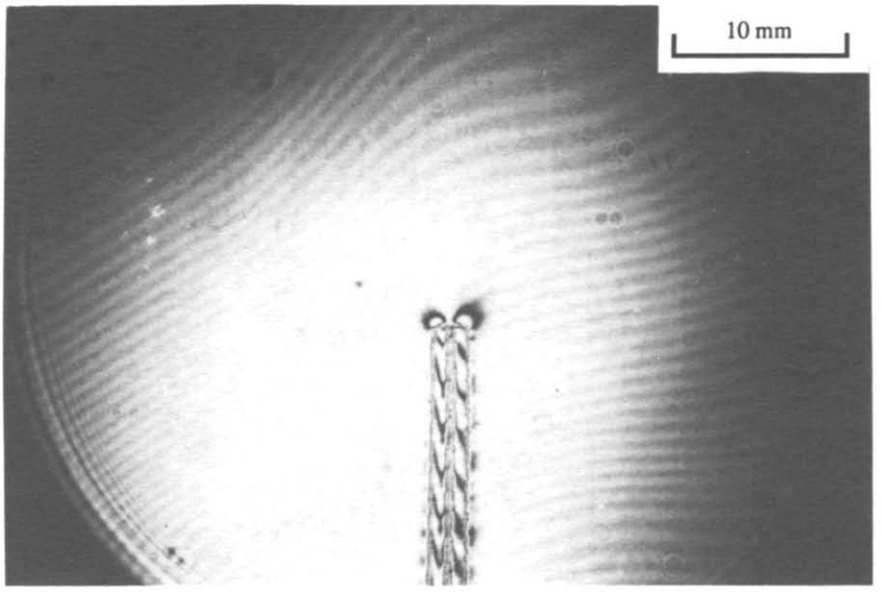

(b)

Fig. 3. Infinite fringe width fields for experiment 2 ($\Delta = 33$ mm, $P = 0$ N): (a) lateral shearing in x_1-direction; (b) lateral shearing in x_2-direction.

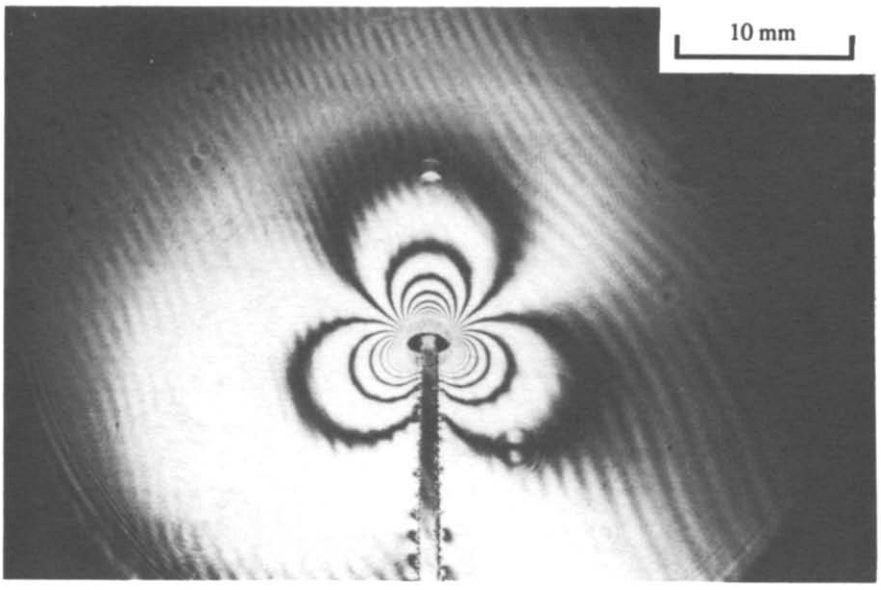

(a)

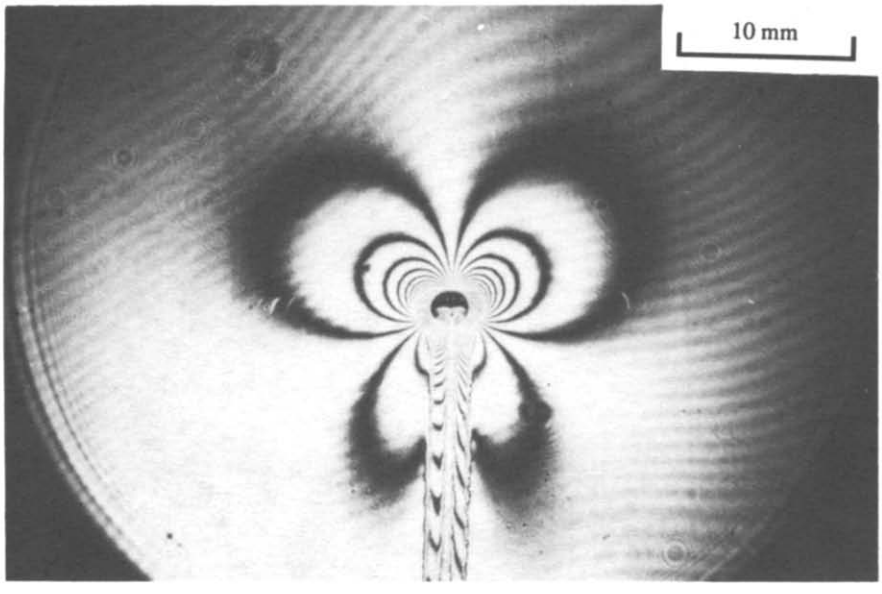

(b)

Fig. 4. Infinite fringe width fields for experiment 2 ($\Delta = 33$ mm, $P = 2230$ N): (a) lateral shearing in x_1-direction; (b) lateral shearing in x_2-direction.

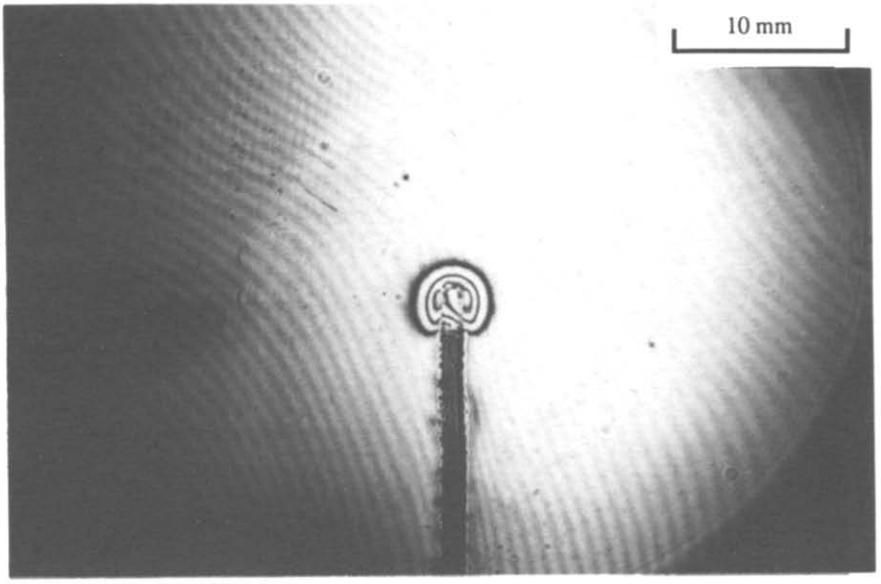

(a)

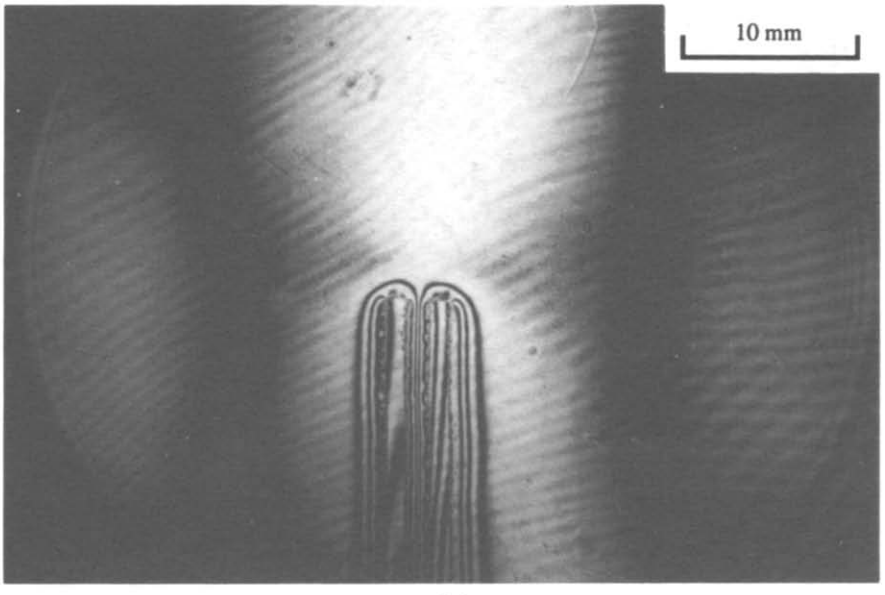

(b)

Fig. 5. Infinite fringe width fields for experiment 2 ($\Delta = 100$ mm, $P = 0$ N): (a) lateral shearing in x_1-direction; (b) lateral shearing in x_2-direction.

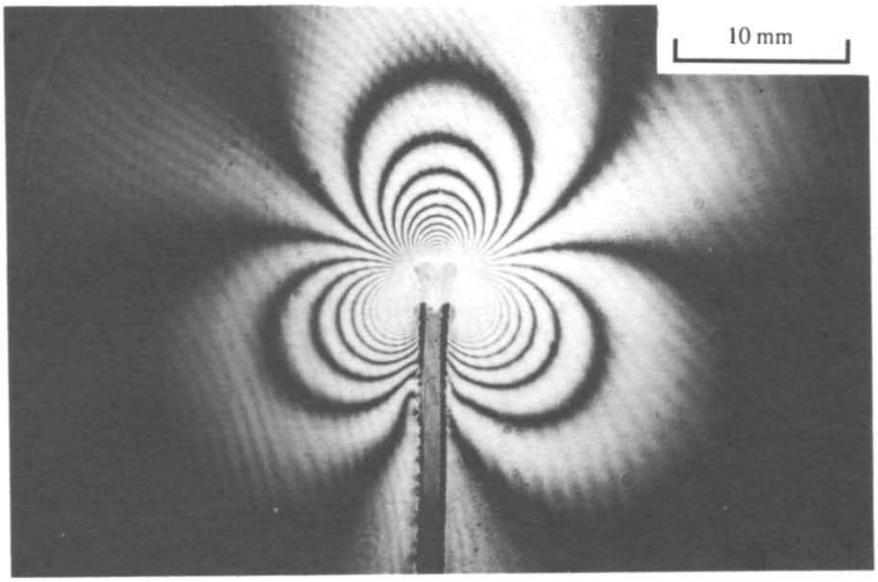

(a)

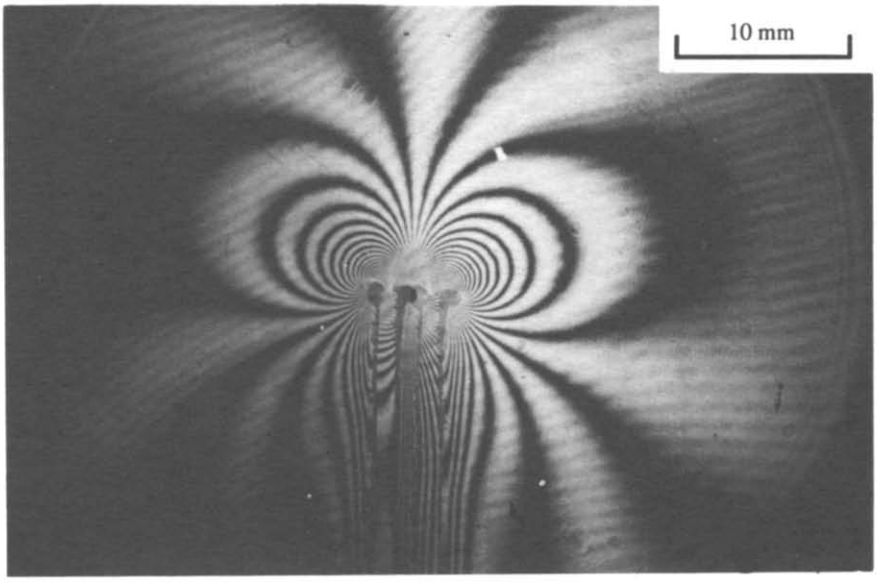

(b)

Fig. 6. Infinite fringe width fields for experiment 2 ($\Lambda = 100$ mm, $P = 2230$ N): (a) lateral shearing in x_1-direction; (b) lateral shearing in x_2-direction.

be defined using the crack tip coordinate system in Fig. 2 as follows:[2]

$$Y^{(\alpha)}(r, \phi) \equiv \left(\frac{mp}{\Delta}\right) \frac{\sqrt{2\pi}}{ch} \frac{r^{3/2}}{\{\delta_{\alpha 1} \cos(3\phi/2) + \delta_{\alpha 2} \sin(3\phi/2)\}}, \qquad \alpha = 1, 2 \tag{1}$$

where

$$r = \sqrt{\left(x_1 + \frac{\Delta\theta_G \cos\theta}{2}\right)^2 + \left(x_2 + \frac{\Delta\theta_G \sin\theta}{2}\right)^2}$$

$$\phi = \tan^{-1}\left(\frac{x_2 + \dfrac{\Delta\theta_G \sin\theta}{2}}{x_1 + \dfrac{\Delta\theta_G \cos\theta}{2}}\right)$$

$\delta_{\alpha\beta}$ is the Kronecker delta, and $\theta = 0°$ for $\alpha = 1$ while $\theta = 90°$ for $\alpha = 2$. It is apparent from the above two equations that when a K-dominant field adequately describes crack tip deformations, then $Y^{(\alpha)}$ is approximately equal to the Mode I stress intensity factor K_I in the region of K-dominance which surrounds the 3D zone.

Alternatively, the K-dominant, physical interpretation of fringe data from Part I of this investigation can be used to define a function $G^{(\alpha)}$ as follows,

$$G^{(\alpha)}(r, \phi) \equiv \left(\frac{q\lambda}{ch}\right) \sqrt{\frac{\pi}{2}} \frac{1}{\left(\dfrac{1}{\sqrt{r_1^{(\alpha)}}} \cos\left(\dfrac{\phi_1^{(\alpha)}}{2}\right) - \dfrac{1}{\sqrt{r_2^{(\alpha)}}} \cos\left(\dfrac{\phi_2^{(\alpha)}}{2}\right)\right)} \tag{2}$$

where

$$r_1 = \sqrt{(x_1 + \Delta\theta_G \cos\theta)^2 + (x_2 + \Delta\theta_G \sin\theta)^2}$$

$$r_2 = \sqrt{x_1^2 + x_2^2}$$

$$\phi_1 = \tan^{-1}\left(\frac{x_2 + \Delta\theta_G \sin\theta}{x_1 + \Delta\theta_G \cos\theta}\right)$$

$$\phi_2 = \tan^{-1}\left(\frac{x_2}{x_1}\right)$$

are evaluated using $\theta = 0°$ for $\alpha = 1$ while $\theta = 90°$ for $\alpha = 2$. Once again, when a K-dominant field adequately describes crack tip deformations, then $G^{(\alpha)}$ is approximately equal to K_I in the region of K-dominance which surrounds the 3D zone.

The values of $Y^{(\alpha)}$ and $G^{(\alpha)}$ measured at various angles and radial positions using only dark fringes from fringe patterns for the first experiment can be seen plotted against normalized radial distance (r/h) in Figs 7 and 8, respectively. Similar plots for the values of $Y^{(\alpha)}$ and $G^{(\alpha)}$ measured using only dark fringes from the fringe patterns obtained in the second experiment can be seen in Figs 9 and 10, respectively.

3.2 Least squares data analysis

From the experimental results in Ref. 2, it appears that a K-dominant region exists for $0{\cdot}5 < (r/h) < 1{\cdot}25$ near crack tips in three-point bend specimens with certain geometries $(a/w = 0{\cdot}2)$. The values of $Y^{(\alpha)}$ that were obtained in this region were within 10% of the calculated K_I^{2D} values. However, in order to properly confirm the existence of the observed K-dominant regions, a least-squares data analysis was performed on the measured $Y^{(\alpha)}$ values assuming that K-dominance was absent and that an unknown number of terms from Williams' expansion for a Mode I crack tip stress field are necessary to describe the stress field near the crack tip of the three-point bend specimen.

For the least-squares data analysis using the geometric interpretation of fringes, if it is assumed that a power series representation for the stress field surrounding a crack tip is valid (see eqn (22) from Part I of this investigation), then eqns (18) and (19) from Part I of this investigation can be used to express Y^1 and Y^2 as,

$$Y^1(r, \phi) = \left(\frac{mp}{\Delta}\right)\frac{\sqrt{2\pi}}{ch}\frac{r^{3/2}}{\cos(3\phi/2)} = \sum_{N=1}^{\infty}\sqrt{2\pi}\,A_N\left(\frac{N}{2}-1\right)r^{\left(\frac{N-1}{2}\right)}\frac{\cos\left(\frac{N}{2}-2\right)\phi}{\cos(3\phi/2)} \tag{3}$$

$$Y^2(r, \phi) \equiv \left(\frac{np}{\Delta}\right)\frac{\sqrt{2\pi}}{ch}\frac{r^{3/2}}{\sin(3\phi/2)} = \sum_{N=1}^{\infty}\sqrt{2\pi}\,A_N\left(\frac{N}{2}-1\right)r^{\left(\frac{N-1}{2}\right)}\frac{\sin\left(\frac{N}{2}-2\right)\phi}{\sin(3\phi/2)} \tag{4}$$

Note that $Y^{(\alpha)}$ are proportional to A_1 or K_I for a K-dominant field and consist of quantities that are measured from the fringe patterns. The right-hand side of the above expression will be denoted by $F^{(\alpha)}(r, \phi; A_1, A_3, \ldots, A_N)$ and will be the least-squares fit used on the experimental data. It is important to note that the second term in the series expansion on the right-hand side of eqns (3) and (4) does not contribute to the gradient interpretation of the fringe data. This is

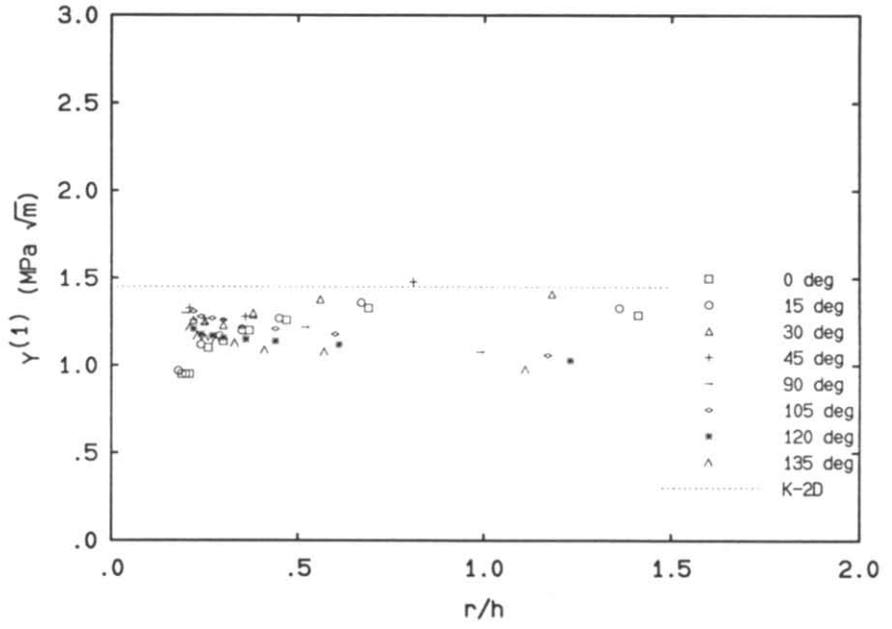

(a)

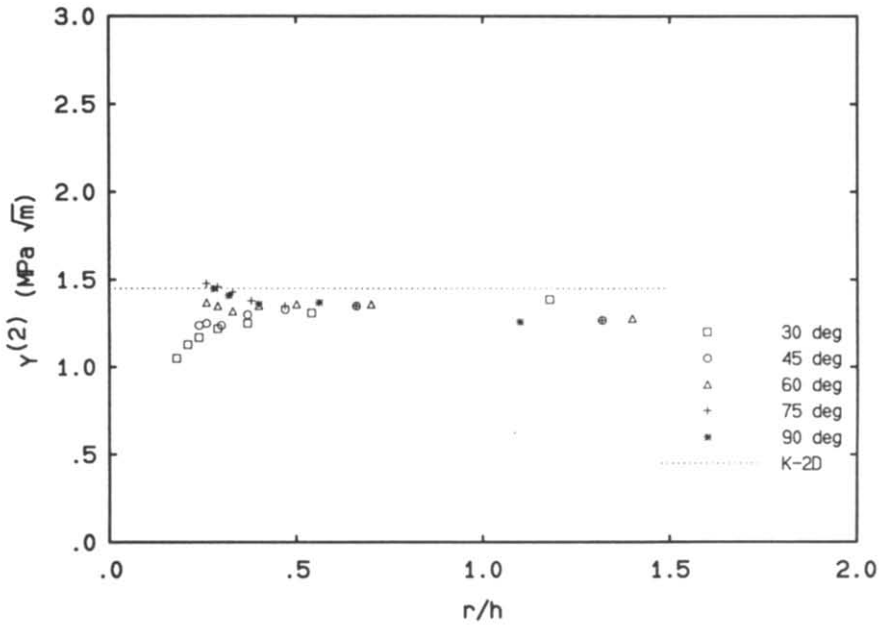

(b)

Fig. 7. Values of $Y^{(\alpha)}$ measured from fringe data from experiment 1 ($\Delta = 33$ mm, $P = 2230$ N).

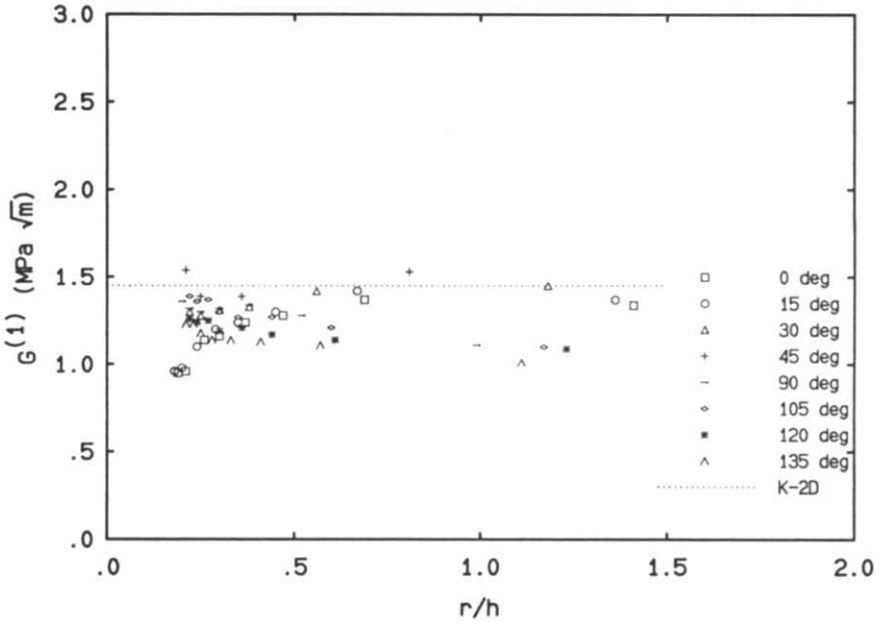

(a)

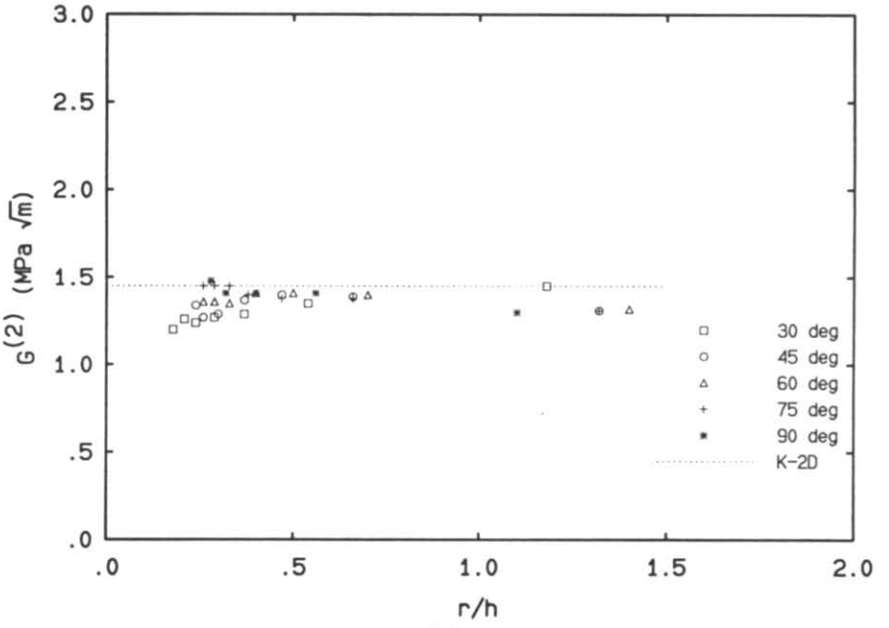

(b)

Fig. 8. Values of $G^{(\alpha)}$ measured from fringe data from experiment 1 ($\Delta = 33$ mm, $P = 2230$ N).

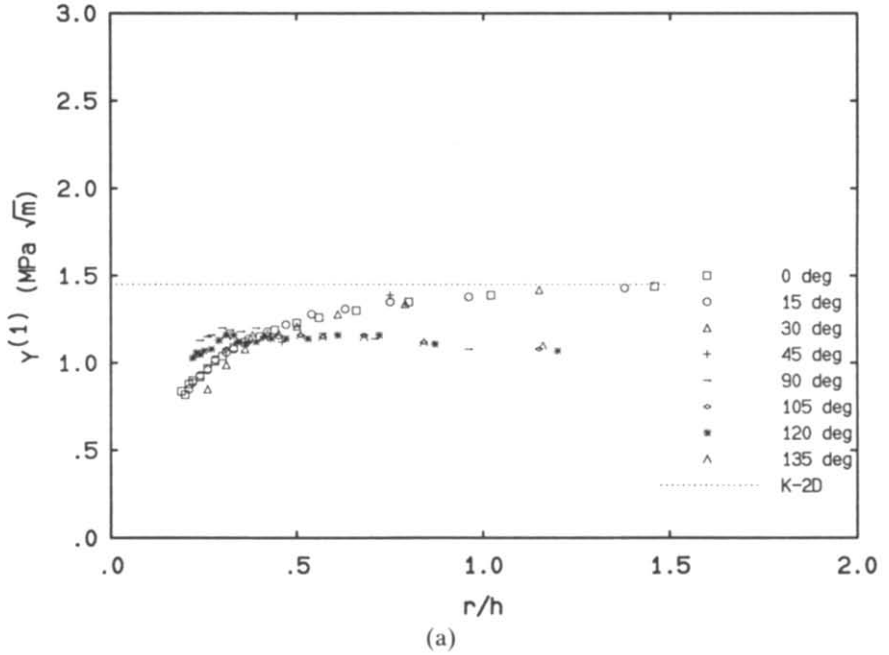

(a)

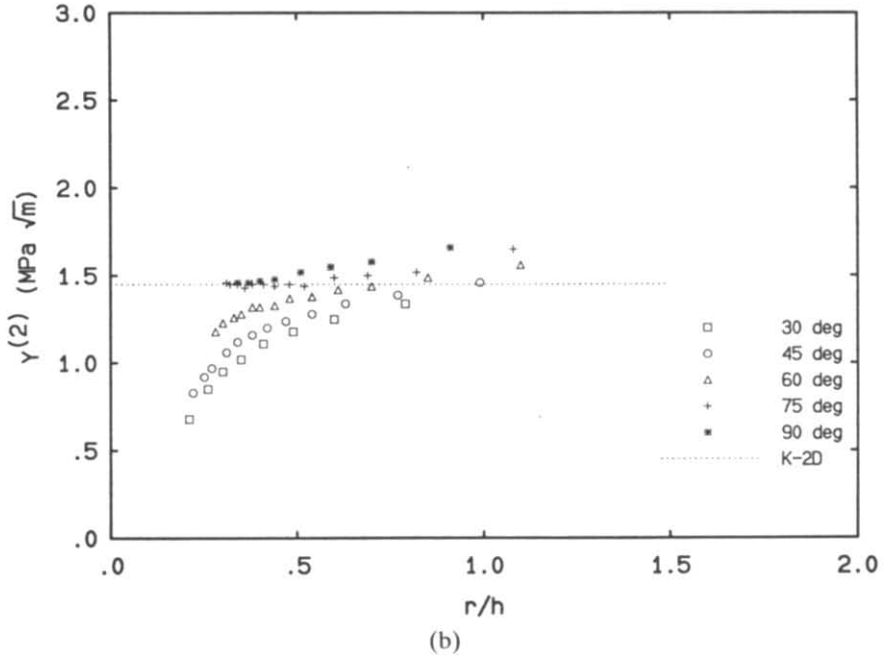

(b)

Fig. 9. Values of $Y^{(\alpha)}$ measured from fringe data from experiment 2 ($\Delta = 100$ m, $P = 2230$ N).

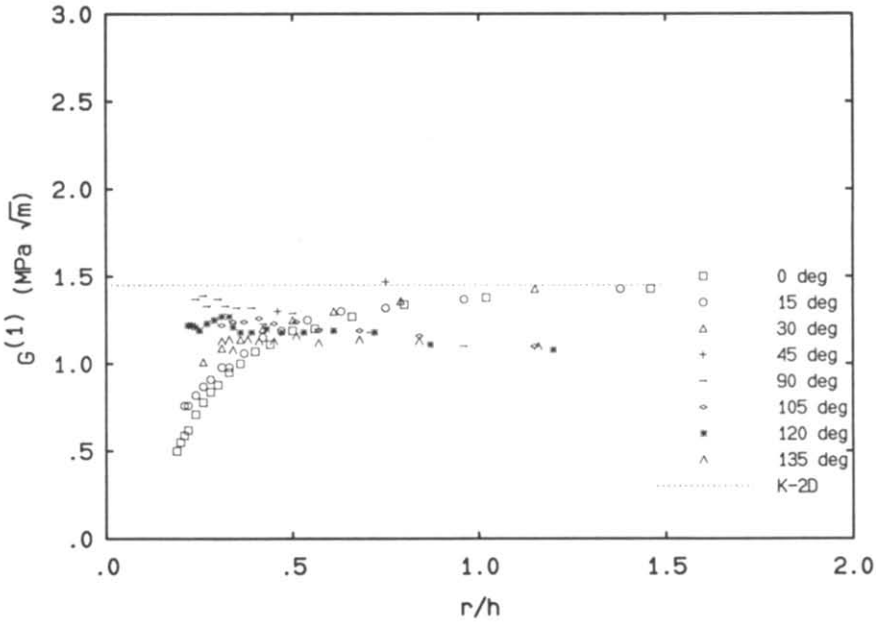

(a)

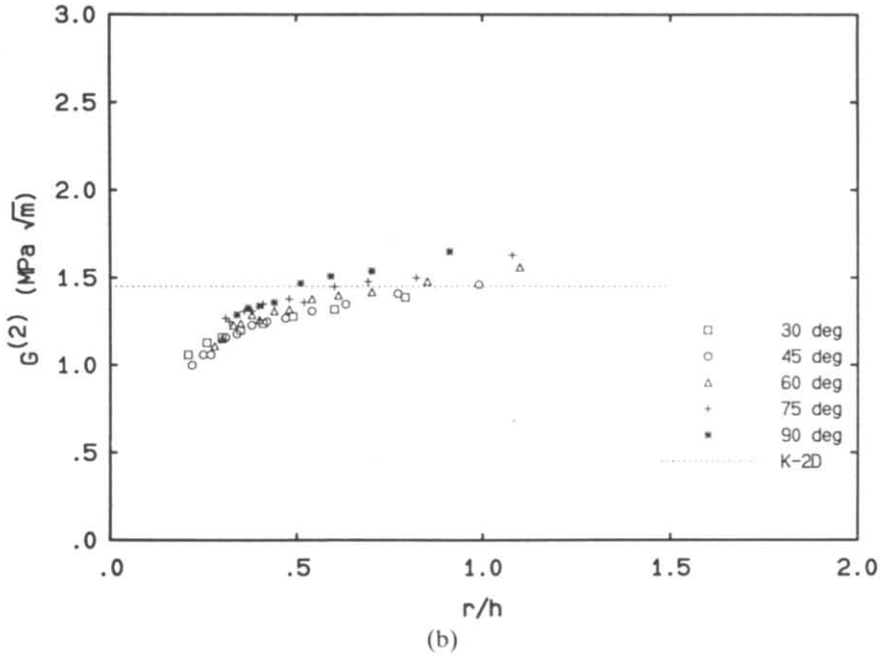

(b)

Fig. 10. Values of $G^{(\alpha)}$ measured from fringe data from experiment 2 ($\Delta = 100$ mm, $P = 2230$ N).

understandable because the second term of the series expansion represents gradients of constant stress, and hence does not contribute to the fringe patterns.

In implementing the curve fitting procedure, the following function $\Phi^{(\alpha)}(A_1, A_3, \ldots, A_N)$ is minimized,

$$\Phi^{(\alpha)}(A_1, A_3, \ldots, A_N) = \sum_{i=1}^{M} [Y_i^{(\alpha)} - F_i^{(\alpha)}]^2 \tag{5}$$

with respect to $A_1, A_3, \ldots, A_N$. Here, M is the total number of data points used in the minimization. The quality of the fit was measured using a normalized cross-correlation error function, $\varepsilon^{(\alpha)}(N)$, as follows,

$$\varepsilon^{(\alpha)}(N) = 1 - \frac{\sum_{i=1}^{M} Y_i^{(\alpha)} F_i^{(\alpha)}}{\sqrt{\sum_{i=1}^{M} (Y_i^{(\alpha)})^2 \sum_{i=1}^{M} (F_i^{(\alpha)})^2}} \tag{6}$$

A normalized cross-correlation value of 0 represents a perfect fit. The values of $\varepsilon^{(\alpha)}(N)$ calculated using the geometric interpretation in the least-squares fit to fringe data obtained from experiments 1 and 2 can be seen in Figs 11 and 12, respectively for values of $N \leq 10$.

In previous experimental CGS work,[2] an error function was used that was normalized by the first term in the series expansion, A_1. By singling out an individual term in a least-squares fit, the resulting error function could not be minimized without biasing the minimization towards least-squares fits that would yield larger values of A_1. Thus, the results from the least-squares fits used on the experimental data in Ref. 2 yielded minimized values for the error function at a finite number of higher order terms. However, the normalized cross-correlation error function seen in eqn (6) will be unbiased towards the contributions of individual terms in the least-squares fits. Consequently, the values of $\varepsilon^{(\alpha)}(N)$ would be expected to decrease continuously as more and more higher order terms are added in the least-squares fit, since the additional terms allow the fitted function $F^{(\alpha)}$ to become more flexible thereby reducing any differences between the experimental data and the optimized fit due to measurement errors in the CGS technique. The error function in eqn (6) should therefore converge rapidly to the number of higher order terms that actually contribute to the experimentally observed stress field, and additional higher order terms should only marginally improve the least-squares fit by compensating for measurement errors in the CGS technique.

For the least-squares data analysis using the physical interpretation of

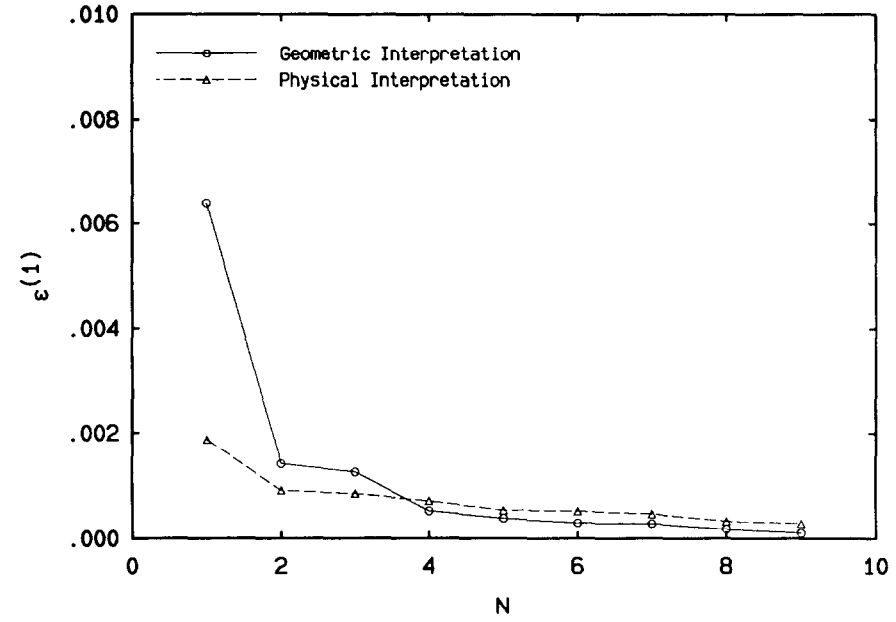

(a)

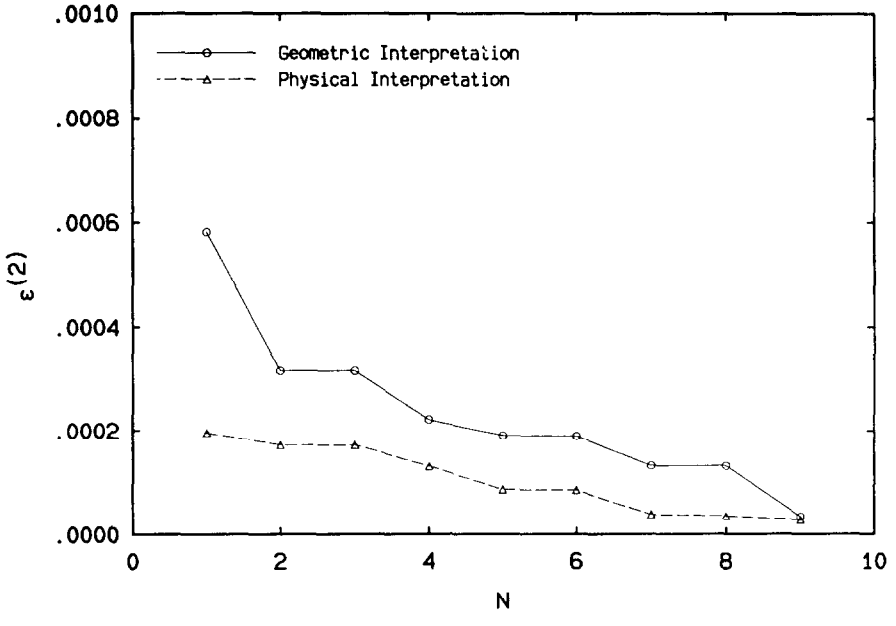

(b)

Fig. 11. Normalized cross-correlation error for least-squares fit to fringe data from experiment 1 ($\Delta = 33$ mm, $P = 2230$ N).

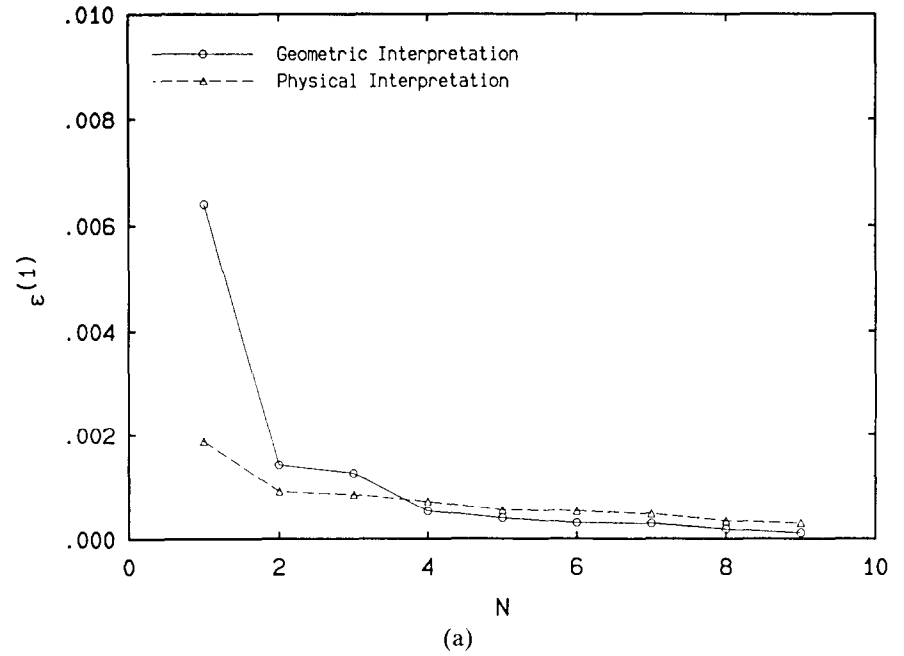

(a)

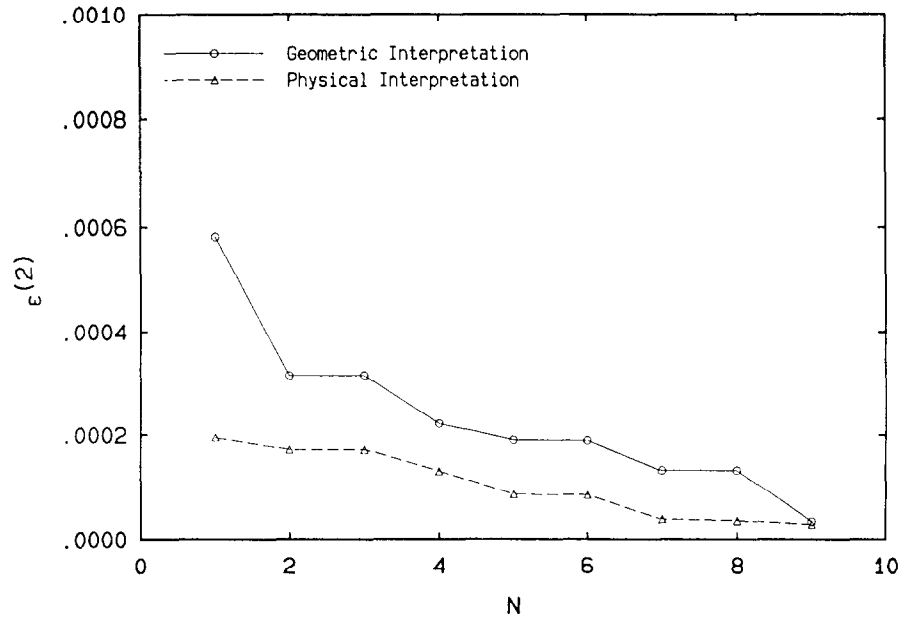

(b)

Fig. 12. Normalized cross-correlation error for least-squares fit to fringe data from experiment 2 ($\Delta = 100$ mm, $P = 2230$ N).

fringes, eqn (22) was substituted into eqn (11) from Part I of this investigation, yielding

$$G^{(\alpha)}(r,\phi)\equiv\frac{q\lambda}{ch}\sqrt{\frac{\pi}{2}}\frac{1}{\left(\frac{1}{\sqrt{r_1^{(\alpha)}}}\cos\left(\frac{\phi_1^{(\alpha)}}{2}\right)-\frac{1}{\sqrt{r_2^{(\alpha)}}}\cos\left(\frac{\phi_1^{(\alpha)}}{2}\right)\right)}$$

$$=\frac{\sum_{N=1}^{\infty}\sqrt{\frac{\pi}{2}}A_N\left((r_1^{(\alpha)})^{(\frac{N}{2}-1)}\cos\left(\frac{N}{2}-1\right)\phi_1^{(\alpha)}-(r_2^{(\alpha)})^{(\frac{N}{2}-1)}\cos\left(\frac{N}{2}-1\right)\phi_2^{(\alpha)}\right)}{\left(\frac{1}{\sqrt{r_1^{(\alpha)}}}\cos\left(\frac{\phi_1^{(\alpha)}}{2}\right)-\frac{1}{\sqrt{r_2^{(\alpha)}}}\cos\left(\frac{\phi_2^{(\alpha)}}{2}\right)\right)} \tag{7}$$

Note that $G^{(\alpha)}$ are proportional to A_1 or K_1 for a K-dominant field and consist of quantities that are measured from the fringe patterns. The left-hand side of eqn (7) will be denoted by $H^{(\alpha)}(r, \phi; A_1, A_3, \ldots, A_N)$ and will be the least-squares fit used on the experimental data. Once again, the second term in the series expansion for the least-squares fit is equal to zero. By substituting $G^{(\alpha)}$ and $H^{(\alpha)}$ for $Y^{(\alpha)}$ and $F^{(\alpha)}$ in eqn (5), the same procedure can be used to optimize the least-squares fit for the physical interpretation CGS fringes as is used for the geometric interpretation of fringes. The values of $\varepsilon^{(\alpha)}(N)$ calculated using the physical interpretation in the least-squares fit to fringe data obtained from experiments 1 and 2 can also be seen in Figs (11) and (12) respectively for values of $N \leq 10$.

4 DISCUSSION OF RESULTS

From Part I of this investigation, it was determined that for a K-dominant region of radius greater than three times the shearing distance, $\Delta\theta$, the errors in using the geometric interpretation of fringe data are less than 5%. Therefore to obtain this level of accuracy experimentally, the region of K-dominance should be greater than $\frac{r}{h}=0{\cdot}28$ for experiment 1 and greater than $\frac{r}{h}=0{\cdot}84$ in experiment 2. Furthermore, lateral shearing effectively extends the apparent dimensions of the 3D affected region on the image plane by $\pm\frac{\varepsilon}{2}$. So, the apparent dimensions of the 3D zone on the image plane should extend out to $\frac{r}{h}=0{\cdot}55$ in experiment 1 and to $\frac{r}{h}=0{\cdot}64$ in experiment 2. The

corresponding number of data points outside of the 3D zone was thereby increased from 14 in Figs 7(a) and 8(a), to 21 in Figs 9(a) and 10(a), while remaining essentially unchanged in Figs 7(b) through 10(b).

It is important to note that before analysing the interpretation of fringe data in Figs 3–6, the fringe width of the infinite fringe width fields at zero load in experiments 1 and 2 was not truly infinite. From Figs 3(a), 3(b) and 5(a), the distance between the dark fringes appears to be approximately 50 mm, or the diameter of the laser beam. From Fig. 5(b), the distance between the dark fringes appears to be approximately 25 mm. These fringes appear because the wave front passing through the unloaded specimen is not truly planar due to imperfections in the collimator and nonuniformity in the specimen's thickness. Also, any misalignment of the diffraction gratings has been shown to produce finite fringe width fields.[8] Subsequently, the fringes from loaded specimens should be interpreted under the restrictions of finite fringe width fields.[9]

In the interpretation of finite fringe width fields, fringes are generated from interfering rays by superposing the optical path differences responsible for the undeformed finite fringe width field with optical path differences due to specimen deformations. As a result, the fringe order is proportional to the displacement of undeformed fringes by the deformed wave front, as opposed to the infinite fringe width field interpretation which assumes optical path differences are due only to specimen deformations. One way of eliminating the effects of the undeformed finite fringe width field is to take digital images of the deformed and undeformed fringe fields and process the images to reverse the effects of superposing optical path differences. However, if it is assumed that the frequency of the fringes in the undeformed finite fringe width field is much lower than the frequency of the fringes in the deformed finite fringe width field, then the effects of the optical path differences responsible for the undeformed finite field can be neglected and an infinite fringe width field interpretation can be used.

From Figs 4 and 6, it is obvious that the frequency of the higher order fringes from the deformed specimen are much higher than the frequency of fringes from the undeformed specimen. Consequently, any ambiguities in interpreting the higher order fringes using an infinite fringe width field are considerably less than the ambiguities in interpreting the lower order fringes. Ambiguities also arise in locating the exact position of minimum or maximum intensity within lower order fringes because the lower frequencies result in larger fringe widths.

The aforementioned ambiguities are immediately evident from the

apparent asymmetries in the location of lower order fringes in Figs 4 and 6. As the fringe order increases approaching the crack tip in these figures, the symmetry of the fringes improves considerably. The end result of these ambiguities is to increase the uncertainty in the measurement of $Y^{(\alpha)}$ and $G^{(\alpha)}$ from the lower order fringes. Thus, there is considerable scatter of the lower order fringe data furthest from the crack tip in Fig. 7 about the 2D value of K_I calculated from the specimen's geometry and loading. However, in Fig. 9(a) the order of the fringe data measured at locations comparable to those in Fig. 7 were much higher because of the increased sensitivity, resulting in much less scatter. In Fig. 9(b), the increased frequency of the finite fringe width field resulted in increased scatter despite the increased sensitivity.

Comparing Fig. 7 with Fig. 8, it is apparent the values of $Y^{(\alpha)}$ and $G^{(\alpha)}$ are nearly identical, which is expected since most of the data were obtained at distances $\frac{r}{h} > 0{\cdot}28$. However, the results from Figs 9 and 10 show a definite deviation between comparable values of $Y^{(\alpha)}$ and $G^{(\alpha)}$ that were obtained at distances $\frac{r}{h} < 0{\cdot}84$, which was also anticipated. In fact, the values of $G^{(2)}$ exhibit much less scatter than comparable values of $Y^{(2)}$ in this region, while the values of $G^{(1)}$ decreased considerably from $Y^{(1)}$ for angles between 0° and 45° and increased for angles between 90° and 135°.

It is also apparent from Figs 7–10 that the observed trends in the measured data are consistent for $Y^{(\alpha)}$ and $G^{(\alpha)}$. From the trends in $Y^{(1)}$, it appears that a K-dominant region exists for angles between 0° and 45° in the region outside the apparent 3D zone, while the trends in $Y^{(2)}$ indicate a K-dominant region for angles between 0° and 90° in the region outside the apparent 3D zone. As was stated previously from the results in Ref. 2, it was anticipated that the region of K-dominance should be present everywhere outside of the 3D zone. However, the results from experiments 1 and 2 indicate that strict K-dominance does not prevail for angles greater than 90°.

The lack of K-dominance is supported by the trends in the normalized cross-correlation error in Figs 11 and 12. For almost all of the least-squares fits, convergence in $\varepsilon^{(1)}(N)$ occurs rapidly after only two terms for both $Y^{(1)}$ and $G^{(1)}$. However, similar convergence rates were also observed in $\varepsilon^{(2)}(N)$ for $Y^{(2)}$ and $G^{(2)}$. The magnitude of the error in the least-squares fit was an order of magnitude less for $\varepsilon^{(2)}(N)$ in experiment 1 than for any of the other fits. This is understandable since

the data outside of the 3D zone in Figs 7(a) and 8(a) exhibit almost no scatter about the predicted K_I value.

In order to evaluate the quality of the least-squares fit, $Y^{(\alpha)}$ was plotted against $F^{(\alpha)}$ for experiments 1 and 2 in Figs 13 and 15, respectively. Also, $G^{(\alpha)}$ was plotted against $H^{(\alpha)}$ for experiments 1 and 2 in Figs 14 and 16, respectively. From the results in Figs 13 and 15, the value of K_I could be determined directly from the convergence of the values of $F^{(\alpha)}$ as $\frac{r}{h}$ approaches 0. However, the value of K_I could not be explicitly determined from $H^{(\alpha)}$ because $H^{(\alpha)}$ does not asymptotically approach K_I as $\frac{r}{h}$ approaches 0. In fact, the value of $H^{(1)}$ oscillates about $\frac{r}{h} \cong 0{\cdot}125$ in Fig. 14(a) and $\frac{r}{h} \cong 0{\cdot}05$ in Fig. 16(a) before converging to approximately 1·30 MPa $\sqrt{\text{m}}$ at $\frac{r}{h} = 0$ in both figures. So, the value of K_I had to be calculated using A_1, which yielded a value of approximately 1·22 MPa $\sqrt{\text{m}}$ from $H^{(1)}$ and $H^{(2)}$ in experiment 1 and values of approximately 1·23 MPa $\sqrt{\text{m}}$ from $H^{(1)}$ and 1·41 MPa $\sqrt{\text{m}}$ from $H^{(2)}$ in experiment 2.

5 CONCLUSIONS

An experimental investigation into the effects of increased sensitivity on the accuracy of the geometric interpretation of fringes obtained from the transmission CGS technique has yielded quantitative and qualitative results for applications to the study of deformations in K-dominant regions near crack tips. The results of increasing the sensitivity are as follows:

(1) More fringes are generated outside of the predicted 3D zone near the crack tip. This results in a higher fringe density and increases the quantity of data that can be measured outside of the 3D region.
(2) The fringes are sharper due to the higher fringe density. This reduces ambiguities in measuring the correct location of the minimum or maximum intensity in the fringe.
(3) The higher fringe density results in higher fringe orders. This also reduces ambiguities in correctly identifying the order of

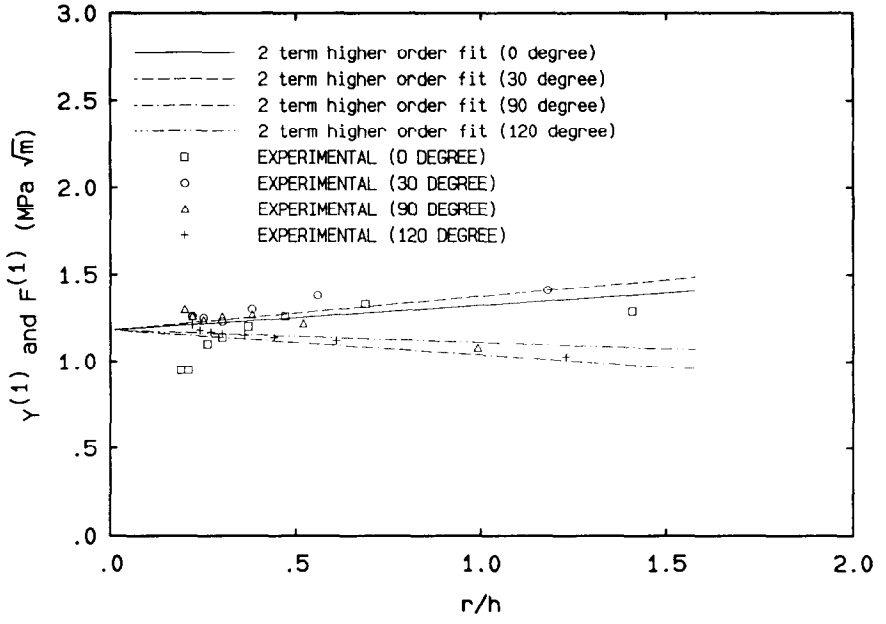

(a)

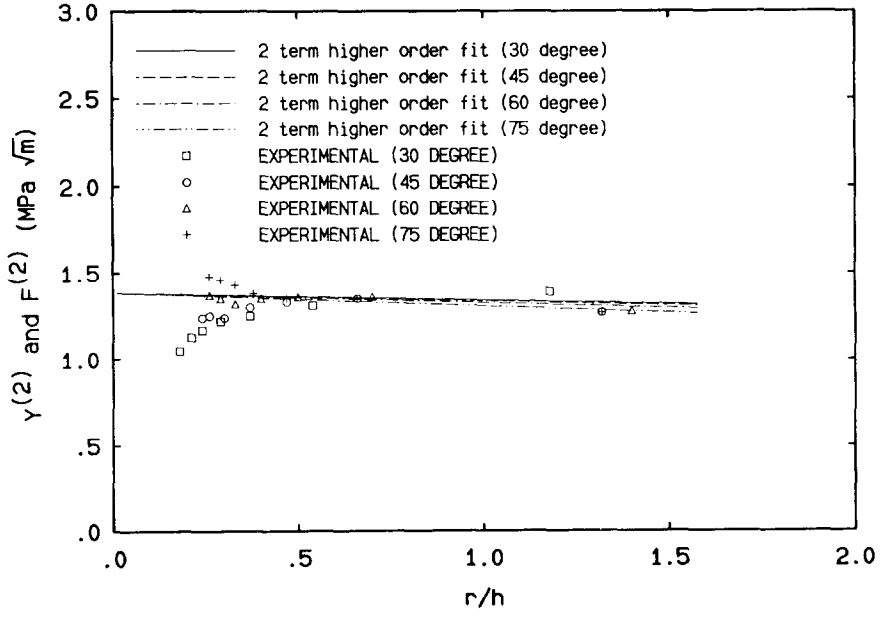

(b)

Fig. 13. Results from least-squares fit to fringe data from experiment 1 ($\Delta = 33$ mm. $P = 2230$ N) using geometric interpretation.

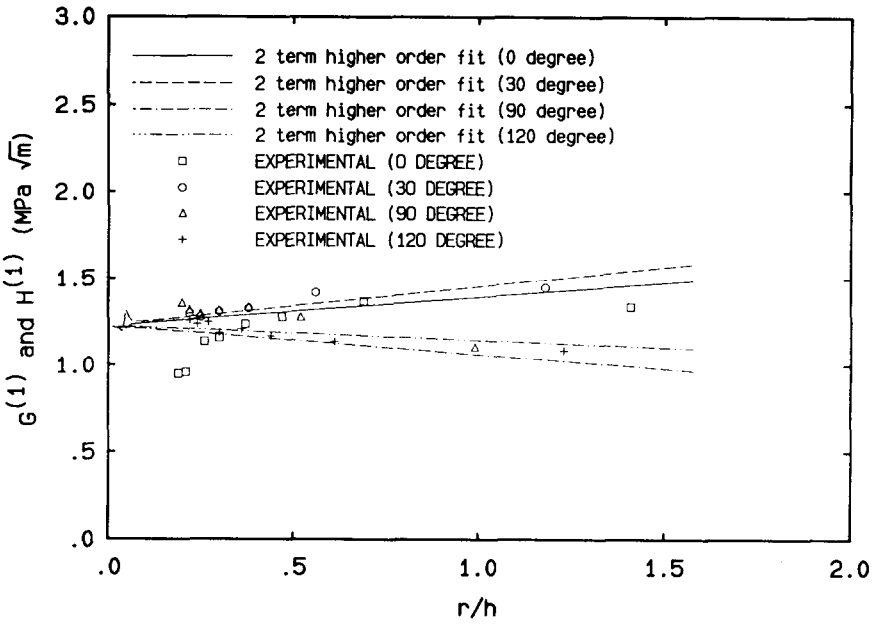

(a)

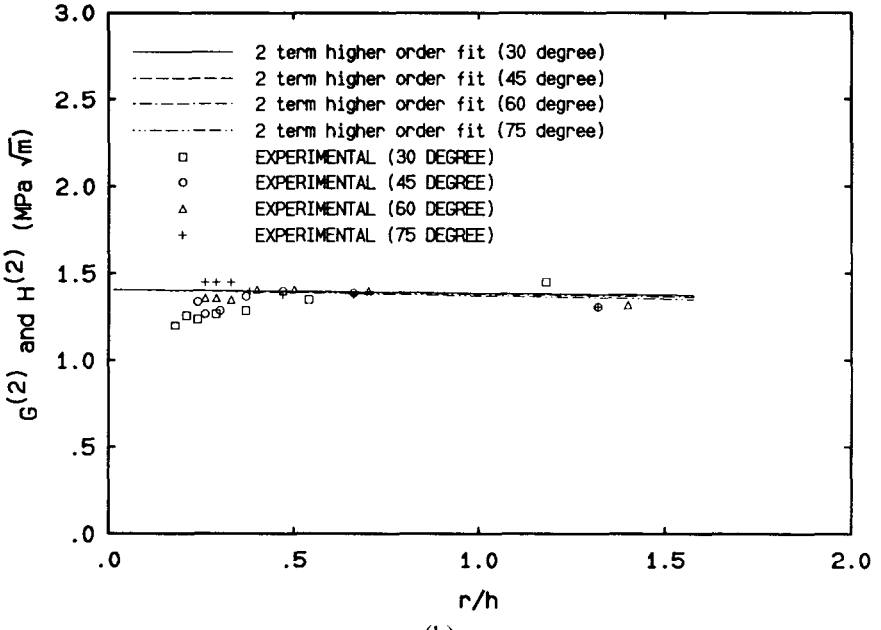

(b)

Fig. 14. Results from least-squares fit to fringe data from experiment 1 ($\Delta = 33$ mm, $P = 2230$ N) using physical interpretation.

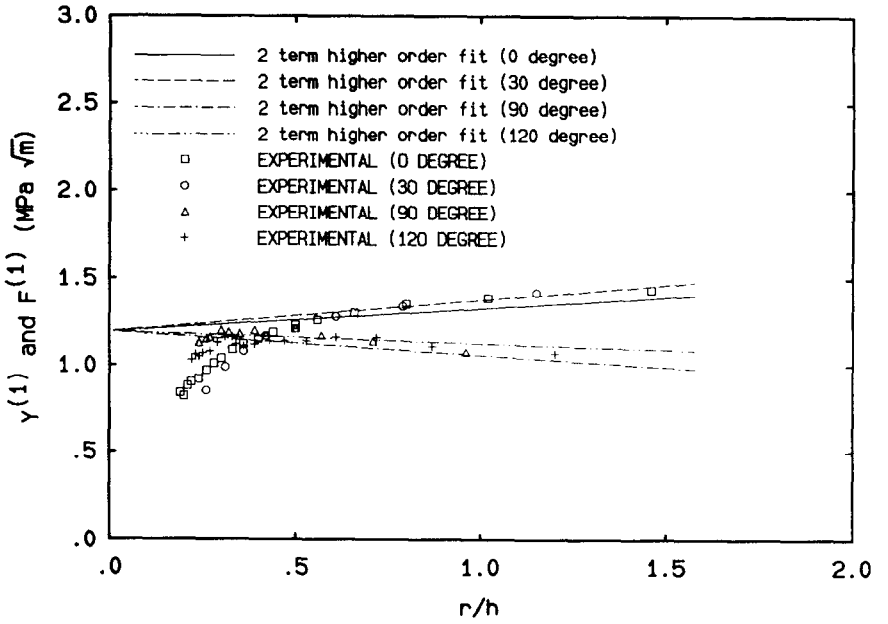

(a)

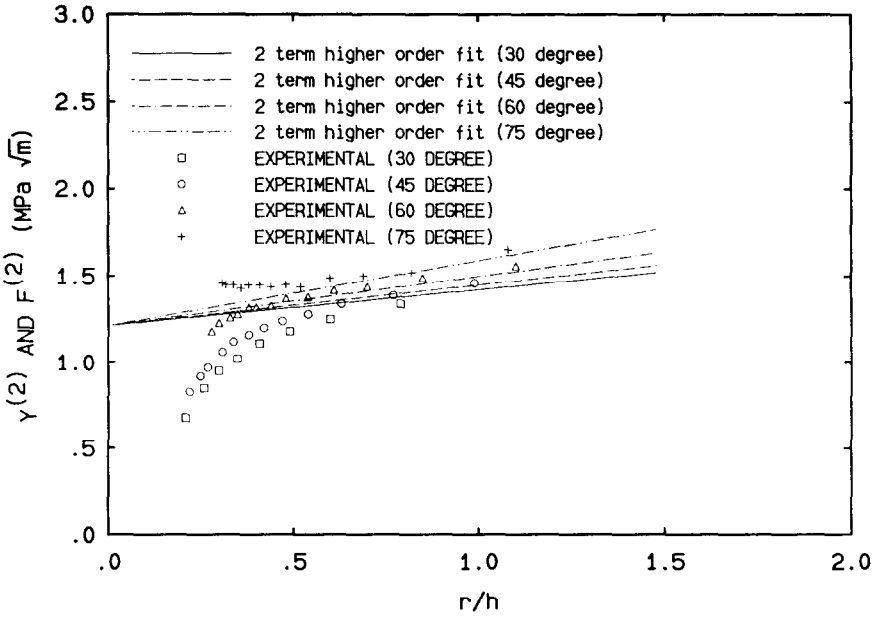

(b)

Fig. 15. Results from least-squares fit to fringe data from experiment 2 ($\Delta = 100$ mm. $P = 2230$ N) using geometric interpretation.

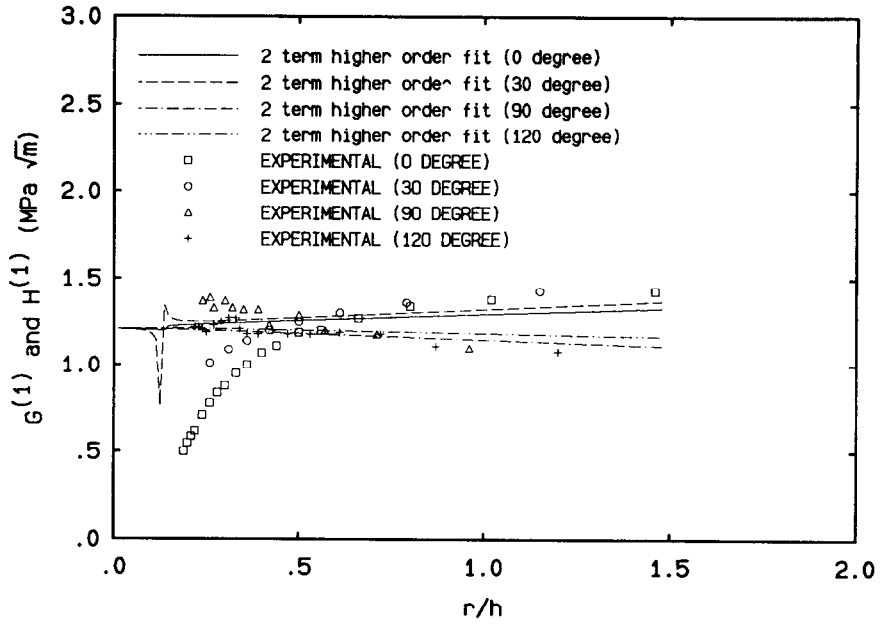

(a)

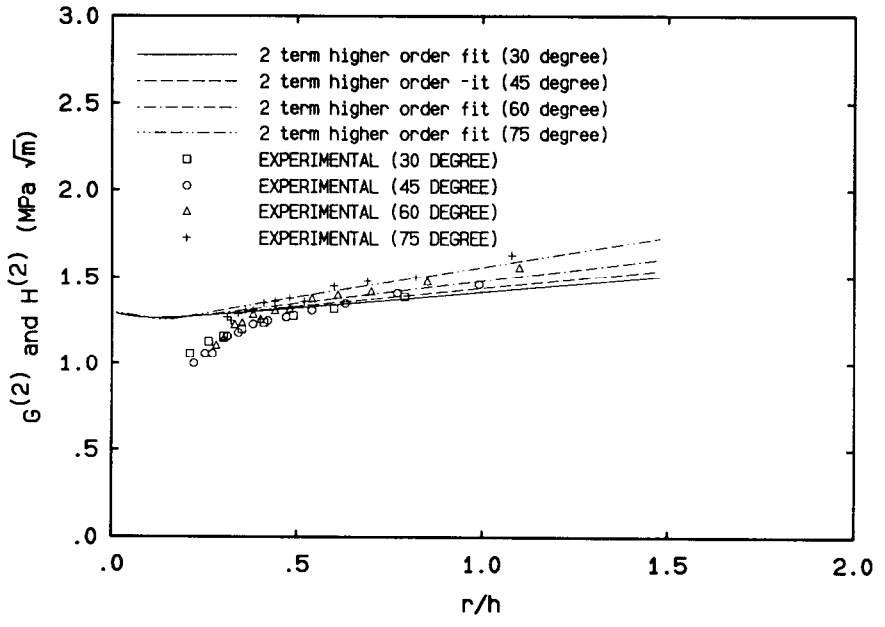

(b)

Fig. 16. Results from least-squares fit to fringe data from experiment 2 ($\Delta = 100$ mm, $P = 2230$ N) using physical interpretation.

fringes assuming an infinite fringe width field as long as the fringes remain inside the field of view. If fringes move outside of the field of view during loading, the fringe order must first be identified when the entire fringe is inside the field of view. Then, the remaining visible portions of the fringe must be tracked during loading in order to reduce ambiguities.

(4) The apparent size of the region on the image plane where the 3D zone affects fringe measurements increases. This is a direct result of the increased lateral shearing necessary for increased sensitivity. However, the increase in the apparent size of the 3D zone is confined to the direction of shearing.

(5) The differences between the geometric and finite difference interpretations of CGS fringe data increased in a larger region about the crack tip as the sensitivity of the CGS technique increased.

From the experimental results given in this paper, it is obvious that the increased sensitivity resulted in more data with improved fringe quality. However, the deformations that were observed near the crack tip did not appear to have a uniform region of K-dominance as evidenced by the least-squares fits.

ACKNOWLEDGEMENTS

Tha authors would like to acknowledge the support of the Office of Naval Research through ONR Grant No. N0014-90-J-1340 (Dr Y. Rajaparke, Program Monitor).

REFERENCES

1. Tippur, H. V., Krishnaswamy, S. & Rosakis, A. J., A coherent gradient sensor for crack tip deformation measurements: analysis and experimental results. *International Journal of Fracture*, **48** (1991) 193–204.
2. Tippur, H. V., Krishnaswamy, S. & Rosakis, A. J., Optical mapping of crack tip deformations using the method of transmission and reflection coherent gradient sensing: a study of crack tip K-dominance. *International Journal of Fracture*, **52** (1991) 91–117
3. Krishnaswamy, S., Tippur, H. V. & Rosakis, A. J., Measurement of transient crack tip deformation fields using the method of coherent gradient sensing. *Journal of Mechanics and Physics of Solids*, **40** (1992) 339–72.
4. Hung, Y. Y. & Taylor, C. E., Speckle-shearing interferometric camera: a tool for measurement of derivatives of surface displacements. *Proceedings of the Society of Photo-Optical Instrumental Engineering*, **41** (1973) 169–75.

5. Hung, Y. Y. & Liang, C. Y., Image shearing camera for direct measurement of surface strains. *Applied Optics*, **18** (1979) 1046–51.
6. Bruck, H. A. & Rosakis, A. J., On the sensitivity of coherent gradient sensing: part I; a theoretical investigation of accuracy in fracture mechanics applications. *Caltech Report SM91-6*, 1991. *Optics and Lasers in Engineering*, **17** (1992) 83–101.
7. Rooke, D. P. & Cartwright, D. J., *Compendium of Stress Intensity Factors*. Her Majesty's Stationery Office, London, 1975.
8. Hariharan, P. & Hegedus, Z. S., Double grating interferometers II. Application to collimated beams. *Optics Communications*, **14** (1975) 148–51.
9. Merzkirch, W., Generalized analysis of shearing interferometers as applied for gas dynamics studies. *Applied Optics*, **18** (1974) 409–13.